Computers and Geotechnics 164 (2023) 105823

Contents lists available at ScienceDirect

Computers and Geotechnics

journal homepage: www.elsevier.com/locate/compgeo

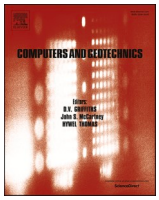

Fully coupled hydro-mechanical modeling of two-phase flow in deformable fractured porous media with discontinuous and continuous Galerkin method

Tianran Ma [a,b], Lintong Jiang [a,c], Weijun Shen [d,*], WenZhuo Cao [e], Chaobin Guo [c], Hamidreza M. Nick [b]

[a] School of Mechanics and Civil Engineering, China University of Mining and Technology, Xuzhou 221116, Jiangsu, China
[b] Danish Offshore Technology Centre, Technical University of Denmark, Kongens Lyngby 2800, Denmark
[c] SinoProbe Laboratory, Chinese Academy of Geological Sciences, Beijing 100037, China
[d] Key Laboratory for Mechanics in Fluid Solid Coupling Systems, Institute of Mechanics, Chinese Academy of Sciences, Beijing 100190, China
[e] Department of Earth Science and Engineering, Imperial College London, London SW7 2BP, United Kingdom

ARTICLE INFO

Keywords:
Two-phase flow
Coupled processes
Discrete fracture network
Discontinuous Galerkin method

ABSTRACT

Discrete fracture and matrix modeling of coupled flow and geomechanics is instrumental for understanding flow in fractured media for various geoengineering applications such as enhanced geothermal energy systems and groundwater remediation. We employ the governing equations for two-phase flow in deformable fractured porous media with a stress-dependent porosity and permeability model of matrix, and variable fracture aperture and the corresponding permeability. A finite element framework is presented, in which fractures are regarded as low-dimensional objects, to discretize the coupled two-phase flow and geomechanics in fractured porous media. A hybrid method, combining discontinuous Galerkin (DG) and continuous Galerkin (CG) finite element methods (FEM), is utilized to solve for the two-phase flow, while the solid deformation is approximated using a discontinuous Galerkin FEM approach. Several benchmark cases are utilized to examine the accuracy of the proposed hybrid DG-CG FEM method. Further validation is performed using more complex, realistic fracture configurations. As the mechanical characteristics of the fracture and the surrounding matrix differ, the simulation results demonstrate that displacement and stress are discontinuous on both sides of the fracture. While the case with low permeability fractures exhibits pressure jump across the fractures, the pressure changes are reasonably smooth for the conduit fractures.

1. Introduction

Coupled hydromechanical processes of fractured porous media are pertinent to a variety of geological applications, including CO_2 storage and sequestration (Wang et al., 2022), enhanced geothermal systems (Salimzadeh et al., 2018; Zheng et al., 2021), and oil or gas production (Jiang and Yang, 2018; Liu et al., 2021; Tian et al., 2023). Fractures occurring at multiple scales with very complex geometries (Salimzadeh et al., 2019b) elevate the difficulty of coupled multi-physics modeling. Discrete fracture models have been proposed for accurate simulations of fluid flow, solid deformation, and their interactions in fractured porous media with variable hydromechanical properties (Latham et al., 2013; Salimzadeh et al., 2019a; Liu, 2022).

In the discrete fracture models, fractures can be represented with lower dimensional entities. Various numerical methods, such as finite element (Ma et al., 2020), finite volume (Reichenberger et al., 2006), extended finite-element (Fumagalli and Scotti, 2013), and finite-volume-finite-element (Matthäi et al., 2010), have been proposed and implemented for both conforming and nonconforming grids. Several new numerical schemes have evolved within the finite volume framework, including the control-volume method (Monteagudo and Firoozabadi, 2004), cell-centered finite volume (CCFV) with two-point flux approximation (TPFA) or multi-point flux approximation (MPFA) (Monteagudo and Firoozabadi, 2004; Gläser et al., 2017; Gläser et al., 2019), vertex-centered finite-volume (VCFV) (Gläser et al., 2022), and projection-based embedded discrete fracture method (pEDFM) (Jiang

* Corresponding author.
E-mail address: wjshen763@imech.ac.cn (W. Shen).

https://doi.org/10.1016/j.compgeo.2023.105823
Received 12 July 2023; Received in revised form 19 September 2023; Accepted 21 September 2023
Available online 29 September 2023

and Younis, 2017; HosseiniMehr et al., 2022). Later, the enriched Galerkin (Kadeethum et al., 2020a) and discontinuous Galerkin finite element (Ma et al., 2021b) have been developed to simulate fluid flow in fractured rocks.

From a mechanical aspect, a fracture is regarded as a mechanical discontinuity that results in the discontinuity of displacement between two sides of the fracture. Zero-thickness interface elements (Nguyen, 2014b; Cerfontaine et al., 2015) and lower-dimensional interface elements with local enrichment approximation (Jafari et al., 2022) are two significant approaches. The interface elements approach was initially presented by Goodman et al. (1968) and has earned a great deal of attention and application in the traditional FEM analyses due to its ease of implementation. The extended finite element method's (XFEM) enrichment approximation employs local enrichment functions, specifically jump functions, within an approximation space. This strategy effectively handles mechanical discontinuities and reduces the costs related to re-meshing associated with fracture growth. Nonetheless, it also expands the degrees of freedom.

In general, the governing equations of coupled flow and geomechanics are solved by combining the previously introduced discretization method (Deb and Jenny, 2017; Wu et al., 2020; Khoei and Saeedmonir, 2021; Ren and Younis, 2021; Shen and Riviere, 2022). Jiang and Yang (2018) used a combination of mimetic finite different (MFD) with finite element method (FEM) to single-phase flow subjected to stress conditions. Obeysekara et al. (2018) presented a coupled scheme by linking control-volume method with finite discrete element method with local mesh refinement technology. Ren et al. (2018) developed the XFEM and pEDFM scheme for handling the two-phase flow in deformable fractures and barriers. Cusini et al. (2021) introduced the FV technique for discretizing fluid field and FE discretization of the solid deformation equation associated with the embedded discrete fracture model (EDFM) and the embedded finite element method (EFEM) enrichment approach, respectively. Besides, Khoei et al. (2016) and Jin and Zoback (2017) applied the XFEM and mixed FEM discretization strategies, respectively, for both fluid and solid physics.

In this paper, we advance our prior research (Ma et al., 2021a; Ma et al., 2021b) to investigate the influence of fractures on fluid flow patterns and solid deformation, utilizing the discontinuous Galerkin (DG) and continuous Galerkin (CG) Finite Element Method (FEM). A finite element discretization for multiphase flow in matrix and fracture, and linear momentum balance equation is introduced. The hydro-mechanical significance of the fracture in flow and deformation is captured by a discrete fracture model with unstructured mesh. We adopt discontinuous Galerkin finite element method (DG-FEM) for discretization of fluid flow in the matrix and solid deformation and continuous Galerkin finite element method (CG-FEM) for fluid flow in both permeable and sealed fractures.

This paper is structured as follows: Section 2 presents the strong and weak forms of coupled two-phase flow and solid deformation of fractured porous media. In Section 3, model implementation in a FE software is briefly introduced. In Section 4, several benchmark cases to examine the accuracy of the proposed method are studied. A case with a more complex fracture configuration is also conducted to demonstrate the applicability of the technique to a more realistic fractured medium. Finally, the conclusions are presented in Section 5.

2. Coupled hydro-mechanical governing equations for two-phase flow in deformable fractured porous media

2.1. Strong form of the coupled HM model

The governing equations of coupled hydro-mechanical model comprise of solid deformation and two-phase flow equations. Under the assumption of quasi-static and linear elasticity, the mechanical equilibrium of solid skeleton is stated as

$$\nabla\cdot\boldsymbol{\sigma}+F=0 \tag{1}$$

where F is the body force, and $\boldsymbol{\sigma}$ is total stress, which includes two parts of contributions from solid skeleton and internal fluids. We assume that a positive stress acts in tension. The total stress $\boldsymbol{\sigma}$ is defined as the function of effective stress $\boldsymbol{\sigma}'$ and means pore pressure p^m, which is defined as:

$$\boldsymbol{\sigma}=\boldsymbol{\sigma}'-\alpha\mathbf{I}p=\mathbb{C}:\boldsymbol{\varepsilon}-\alpha\mathbf{I}p^m \tag{2}$$

where $\mathbb{C}$ is four-order elasticity tensor, α is the Biot's coefficient of porous media, and $\mathbf{I}$ is the identity tensor. The gradient of the displacement $\boldsymbol{u}$ is related to the symmetric elastic strain $\boldsymbol{\varepsilon}$

$$\boldsymbol{\varepsilon}=\frac{1}{2}\left(\nabla\boldsymbol{u}+\nabla\boldsymbol{u}^T\right) \tag{3}$$

The fractures might be either open or closed. Typically, as the fracture closes, the Coulomb model is employed to describe frictional sliding (Nguyen, 2014a; Cusini et al., 2021). In this work, we focus exclusively on the condition that fracture aperture size remains larger than zero. Without considering the contact conditions on the fracture the traction balance on the fracture surface is described by effective contact tractions $\boldsymbol{\sigma}^f$ and fracture pressure p^f,

$$[\![\boldsymbol{\sigma}^f]\!]=[\![\boldsymbol{\sigma}^f-\alpha\mathbf{I}p^f]\!]=0 \tag{4}$$

where $[\![\boldsymbol{\sigma}^f]\!]$ represents the stress jump across the fracture. Eq. (4) enforces the continuity of the stresses across the fracture. The effective stress $\boldsymbol{\sigma}^f$ is determined by

$$\boldsymbol{\sigma}^f=\boldsymbol{S}[\![\boldsymbol{u}]\!] \tag{5}$$

where $[\![\boldsymbol{u}]\!]$ is the relative displacement or displacement jump across the fracture, the stiffness tensor $\boldsymbol{S}$ is given as

$$\boldsymbol{S}=\begin{bmatrix}S_{tt} & 0\\ 0 & S_{nn}\end{bmatrix} \tag{6}$$

where S_{tt} and S_{nn} represent the shear and normal stiffness of fractures, respectively. When there is no contact between the two sides of a fracture, the sole pressure extended by fluids causes fracture to split and impacts the stress (Cusini et al., 2021). In this situation, the mechanical characteristics are disregarded, such that S_{tt} and S_{nn} are considered to be zero.

The mass continuity equations for two-phase flow in deformable fractured porous media include three portions: fluid flows in the matrix, fluid flows in fractures, and mass transmission between the matrix and fractures. The governing equations for two-phase flow in the matrix are given by (Ma et al., 2021b)

$$\begin{aligned}\phi^m S_w^m\rho_w^m c_w\frac{\partial p_{nw}^m}{\partial t}+\left(\phi^m\rho_w^m-\phi^m S_w^m\rho_w^m c_w\left|p_c^m\right|\right)\frac{\partial S_w^m}{\partial t}-S_w^m\rho_w^m\frac{S}{K}\frac{\partial\sigma_m'}{\partial t}\\ +\nabla\cdot\left(-\rho_w^m\frac{\boldsymbol{k}^m k_{rw}^m}{\mu_w}\nabla p_{nw}^m\right)-\nabla\cdot\left(-\rho_w^m\frac{\boldsymbol{k}^m k_{rw}^m}{\mu_w}\left|p_c^m\right|\nabla S_w^m\right)=0\end{aligned} \tag{7}$$

$$\phi^m S_{nw}^m\rho_{nw}^m c_{nw}\frac{\partial p_{nw}^m}{\partial t}-\phi^m\rho_{nw}^m\frac{\partial S_w^m}{\partial t}-S_{nw}^m\rho_{nw}^m\frac{S}{K}\frac{\partial\sigma_m'}{\partial t}+\nabla\cdot\left(-\rho_{nw}^m\frac{\boldsymbol{k}^m k_{mw}^m}{\mu_{mw}}\nabla p_{nw}^m\right)=0 \tag{8}$$

and fluid flow in fractures are characterized as

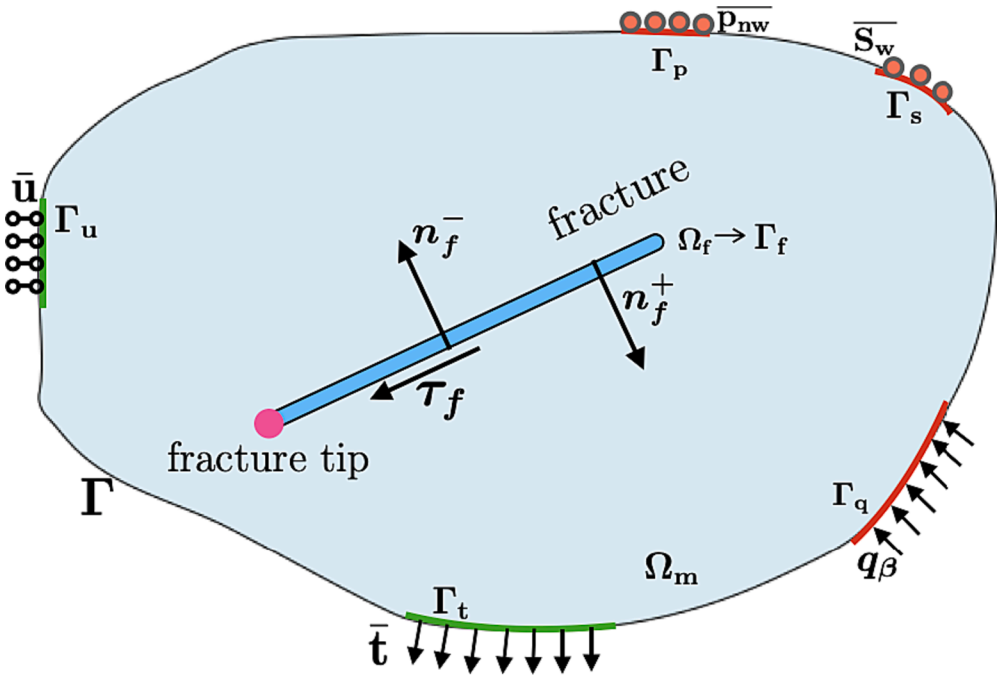

Fig. 1. Diagram of fractured porous media and the boundary conditions. A fracture Ω_f embedded in a region of porous media Ω_m with an external boundary Γ. The fracture Ω_f is considered as a lower-dimensional individual Γ_f with tangential vector τ_f and unit normal vectors n_f^- and n_f^+ on the fracture surface. The Γ_u and Γ_t are the displacement and stress boundaries for the solid component; Boundary conditions of flow problems include flow rate boundary Γ_q, pressure boundary Γ_p, and saturation boundary Γ_s.

$$d^f \phi^f S_w^f \rho_w^f c_w \frac{\partial p_{nw}^f}{\partial t} + d^f \left(\phi^f \rho_w^f - \phi^f S_w^f \rho_w^f c_w |p_c^f|\right) \frac{\partial S_w^f}{\partial t} + d^f \alpha \rho_w^f S_w^f \frac{\partial \varepsilon_n}{\partial t} + \nabla \cdot \left(- d^f \rho_w^f \frac{\boldsymbol{k}_\tau^f k_{rw}^f}{\mu_w} \nabla p_{nw}^f \right) - \nabla_\tau \cdot \left(- d^f \rho_w^f \frac{\boldsymbol{k}_\tau^f k_{rw}^f}{\mu_w} |p_c^f| \nabla S_w^f \right) = [\![\rho_w^m \boldsymbol{v}_w^m]\!] \tag{9}$$

$$d^f \phi^f S_{nw}^f \rho_{nw}^f c_{nw} \frac{\partial p_{nw}^f}{\partial t} - d^f \phi^f \rho_{nw}^f \frac{\partial S_{nw}^f}{\partial t} + d^f \alpha \rho_{nw}^f S_{nw}^f \frac{\partial \varepsilon_n}{\partial t} + \nabla_\tau \cdot \left(- d^f \rho_{nw}^f \frac{\boldsymbol{k}_\tau^f k_{rnw}^f}{\mu_{nw}} \nabla p_{nw}^f \right) = [\![\rho_{nw}^m \boldsymbol{v}_{nw}^m]\!] \tag{10}$$

where the superscripts $\theta = f$ and m signify matrix and fracture variables, respectively. Subscripts $\beta = nw$ and w denote the nonwetting and wetting phase variables, respectively. S_β^θ is the saturation, ρ_β^θ is the fluid density, c_β is the compressibility of fluid, p_β^θ is fluid pressure of each phase, $\boldsymbol{k}^\theta$ is the intrinsic permeability tensor, μ_β is the fluid viscosity, ε_n is normal strain on the fracture, $\boldsymbol{k}_\tau^f$ is fracture permeability in tangential direction, p_c^θ is capillary pressure, which is calculated by $p_{nw}^\theta - p_w^\theta = pe^\theta \left(se^\theta\right)^{-1/0.457}$. se^θ is effective saturation. The relative permeability functions is presented as follows (Pruess et al., 1999):

$$k_{rw}^\theta = \begin{cases} \sqrt{se^\theta} \left[1 - \left(1 - se^{\theta 1/0.8}\right)^{0.8}\right]^2, & if S_w^\theta < 1 \\ 1, & if S_w^\theta > 1 \end{cases} \tag{11}$$

$$k_{rnw}^\theta = \begin{cases} 1 - k_{rw}^\theta, & if S_{nw}^\theta = 0 \\ \left(1 - se^\theta\right)^2 \left(1 - se^{\theta 2}\right), & if S_{nw}^\theta > 0 \end{cases} \tag{12}$$

where k_{rw}^θ and k_{rnw}^θ are the relative permeability of wetting phase and non-wetting phase, respectively. The source or sink terms $[\![\rho_\beta^\theta \boldsymbol{v}_\beta^\theta]\!]$ in Eqs. (9) and (10) is the normal flux transmission between matrix and fractures, which is given by (Aghili et al., 2019; Gläser et al., 2019)

$$[\![\rho_\beta^m \boldsymbol{v}_\beta^m]\!] = - \frac{k_n^f k_{r\beta}^f}{\mu_\beta} \left(\frac{p_\beta^{m+} + p_\beta^{m-} - 2p_\beta^f}{d^f/2} \right) \tag{13}$$

where $\boldsymbol{v}_\beta^m$ is the fluid velocity, k_n^f is the normal fracture permeability, p_β^{m+} and p_β^{m-} are the fluid pressure of each phase β on each side of fracture, respectively. The porosity ϕ^m and permeability k^m of the matrix are affected with the effective stress, as shown by the following equations (Ma et al., 2017):

$$\phi^m = \alpha + S \tag{14}$$

$$k^m = k^{m0} \left(\frac{\phi^m}{\phi^{m0}} \right)^3 = k^{m0} \left(\frac{\alpha + S}{\phi^{m0}} \right)^3 \tag{15}$$

where S is calculated by $\left(\phi^{m0} - \alpha\right) \exp\left(-\frac{\Delta \sigma_m'}{K}\right)$, ϕ^{m0} and k^{m0} are the porosity and permeability of the matrix at the initial stress state, $\Delta \sigma_m'$ is the mean effective stress change between current and initial stress state, K is the bulk modulus of the solid skeleton.

The variation of fracture permeability k^f is described using the cubic law (Yan et al., 2019)

$$k^f = k^{f0} \left(\frac{d^f}{d^{f0}} \right)^2 \tag{16}$$

where d^{f0} and d^f represent fracture aperture at the initial state and the current time step, respectively. We assume that the shear-induced dilation has a negligible impact on the aperture (Segura and Carol, 2008) and focus primarily on the effect of shear deformation on the fracture aperture. Under the above-mentioned assumption, fracture aperture d^f is given as:

$$d^f = d^{f0} + [\![\boldsymbol{u}_n]\!] \cdot \boldsymbol{n}_n \tag{17}$$

where $[\![\boldsymbol{u}_n]\!] \cdot \boldsymbol{n}_n$ denotes the displacement jump between two sides of the

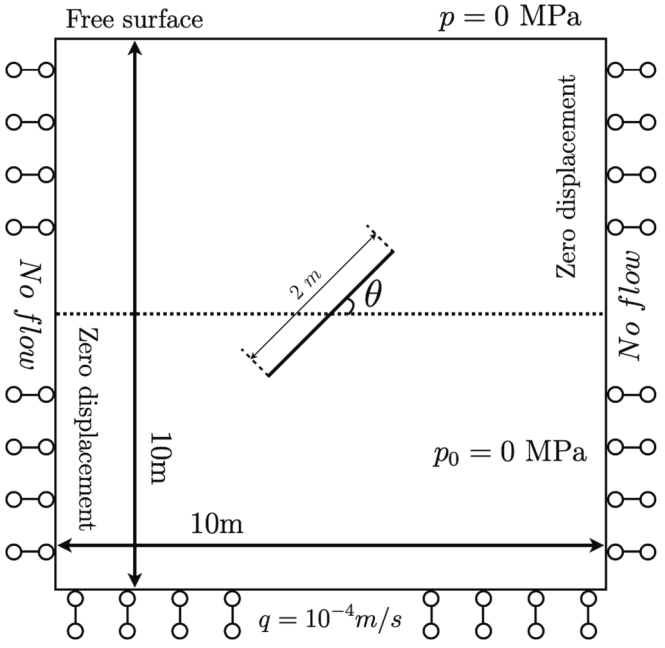

Fig. 2. The geometry, boundary, and initial conditions for test case 1. A single fracture is inside a square domain with an angle of θ with respect to the horizontal axis. The initial pore pressure is zero. The mechanical boundary conditions include free surface at the top boundary and zero displacement at the other boundaries. Boundary conditions of fluid flow include no flow at the left and right boundaries, constant pore pressure, and constant injection rate applied to the top and bottom boundaries, respectively.

fracture in the normal direction. In this model, the fracture porosity ϕ^f is considered to have a constant value of 1 attributed to be the fact that the fracture is addressed as a separate entity.

2.2. Weak form of the coupled HM model

Fig. 1 displays an arbitrary two-dimensional region $\Omega_m \subset \mathbb{R}^2$ bounded with an exterior boundary Γ and with a fracture Ω_f. The fracture Ω_f is represented by a low dimensional object $\Gamma_f \subset \mathbb{R}^1$ due to the disparity in scale between the aperture of fracture and the size of matrix. On the geomechanial boundaries Γ_u and Γ_t, the displacement $\overline{u}$ and stress $\bar{t}$ are applied as:

$$\boldsymbol{u} = \overline{\boldsymbol{u}} \text{on} \Gamma_u \tag{18}$$

$$\boldsymbol{\sigma} \cdot \boldsymbol{n} = \bar{\boldsymbol{t}} \text{on} \Gamma_t \tag{19}$$

For the flow equation, fluid flows into or out of the matrix from the boundary Γ_q at a constant rate of q_β, while pressure $\overline{p_{nw}}$ and saturation $\overline{S_w}$ are fixed on the boundaries Γ_p and Γ_s, respectively.

$$\mathbf{q}_\beta \cdot \boldsymbol{n} = \overline{q_\beta} \text{on} \Gamma_q \tag{20}$$

$$p_{nw} = \overline{p_{nw}} \text{on} \Gamma_p \tag{21}$$

$$S_w = \overline{S_w} \text{on} \Gamma_s \tag{22}$$

We subdivide polygonal domain $\Omega_m \subset \mathbb{R}^2$ into triangular elements E. Let $\mathscr{T} = \mathrm{U}\{E\}$ denote a subset of the matrix domain. The fracture $\Gamma_f \subset \mathbb{R}^1$ is discretized into segment element L. Let $\chi = \mathrm{U}\{L\}$ denote a subdivision inside the fracture domain. The subspaces of the discontinuous finite element for displacement, the non-wetting pressure and wetting saturation of the matrix are specified as follows:

$$Q_u^{DG}(\mathscr{T}) = \left\{ \widetilde{\boldsymbol{u}} \in L_2(\Omega_m) : \widetilde{\boldsymbol{u}}|_E \in p_{r1}(E), \forall E \in \mathscr{T} \right\} \tag{23}$$

$$Q_s^{DG}(\mathscr{T}) = \left\{ \widetilde{S_w^m} \in L_2(\Omega_m) : \widetilde{S_w}|_E \in p_{r2}(E), \forall E \in \mathscr{T} \right\} \tag{24}$$

$$Q_p^{DG}(\mathscr{T}) = \left\{ \widetilde{p_{nw}^m} \in L_2(\Omega_m) : \widetilde{S_{pw}}|_E \in p_{r3}(E), \forall E \in \mathscr{T} \right\} \tag{25}$$

The spaces of the continuous finite element for the pressure and saturation of the fracture are defined as follows:

$$Q_s^{CG}(\chi) = \left\{ \widetilde{S_w^f} \in C_2(\Gamma_f) : \widetilde{S_w^f}|_E \in p_{r4}(L), \forall L \in \chi \right\} \tag{26}$$

$$Q_p^{CG}(\chi) = \left\{ \widetilde{p_{nw}^f} \in C_2(\Gamma_f) : \widetilde{p_{nw}^f}|_E \in p_{r5}(L), \forall L \in \chi \right\} \tag{27}$$

where $p_{r1}(E)$, $p_{r2}(E)$, $p_{r3}(E)$, $p_{r4}(S)$ and $p_{r5}(S)$ represent the space of piecewise polynomials with maximum degree of r_1, r_2, r_3, r_4 and r_5, $L_2(\Omega_m)$ is the space of square integrable function, $C_2(\Gamma_f)$ is the space of vector-valued function. Let $e = \Gamma \cup \Gamma_f \cup \Gamma_m$ symbolize the set of exterior boundaries Γ, internal fracture boundary Γ_f and the interior edges Γ_m of $\mathscr{T}$. We have $\Gamma = \Gamma_u \cup \Gamma_t$ and $\Gamma = \Gamma_q \cup \Gamma_p \cup \Gamma_s$ for the mechanical and flow problems, respectively.

In accordance with the derivation process of our previous work (Ma et al., 2021a; Ma et al., 2021b), the discontinuous Galerkin formation of solid deformation is provided by.

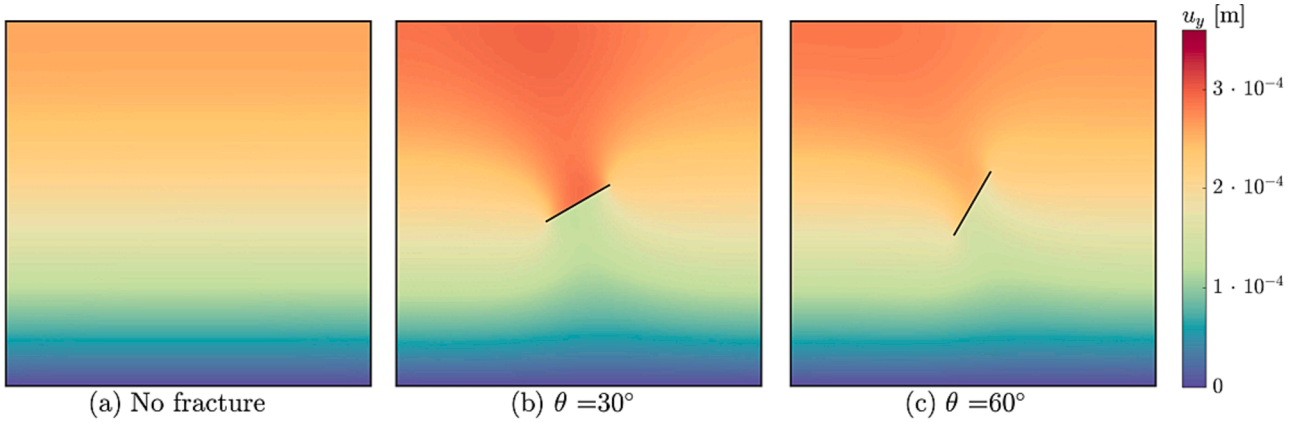

Fig. 3. Distribution of vertical displacement for three different configurations: (a) without fractures in porous media; (b) and (c) include a single fracture with angle $\theta = 30^\circ$ and 60°, respectively.

$$\sum_{E\in\mathcal{T}}\int_E \boldsymbol{\sigma}' : \boldsymbol{\varepsilon}(\widetilde{\boldsymbol{u}})dV - \sum_{E\in\mathcal{T}}\int_E \alpha\mathbf{I}p : \boldsymbol{\varepsilon}(\widetilde{\boldsymbol{u}})dV - \sum_{e\in\Gamma_m\cup\Gamma_u}\int_e \{\boldsymbol{\sigma}'(\boldsymbol{u}) - \alpha\mathbf{I}p^m\}\cdot\boldsymbol{n}[\![\widetilde{\boldsymbol{u}}]\!]dS + \omega_s\sum_{e\in\Gamma_m\cup\Gamma_u}\int_e \{\boldsymbol{\sigma}'(\widetilde{\boldsymbol{u}}) - \alpha\mathbf{I}p^m\}\cdot\boldsymbol{n}[\![\boldsymbol{u}]\!]dS + \sum_{e\in\Gamma_m\cup\Gamma_u}\int_e \frac{G\delta_s}{h}[\![\boldsymbol{u}]\!]\cdot[\![\widetilde{\boldsymbol{u}}]\!]dS$$
$$= \sum_{e\in\Gamma}\int_e (\boldsymbol{\sigma}^f(\boldsymbol{u}) - \alpha\mathbf{I}p^f)\cdot[\![\widetilde{\boldsymbol{u}}]\!]dS + \sum_{E\in\mathcal{T}}\int_E F\widetilde{\boldsymbol{u}}dV + \sum_{e\in\Gamma_t}\int_e \bar{\boldsymbol{t}}\cdot\widetilde{\boldsymbol{u}}dS + \omega_s\sum_{e\in\Gamma_u}\int_e (\boldsymbol{\sigma}'(\widetilde{\boldsymbol{u}}) - \alpha\mathbf{I}p^m)\cdot\boldsymbol{n}\bar{\boldsymbol{u}}dS + \sum_{e\in\Gamma_u}\int_e \frac{G\delta_s}{h}\widetilde{\boldsymbol{u}}\cdot\bar{\boldsymbol{u}}dS \tag{28}$$

The weak forms of fluid flow in the matrix are depicted as

$$\sum_{E\in\mathcal{T}}\int_E\Big[\phi^m S_w^m\rho_w^m c_w\frac{\partial p_{nw}^m}{\partial t} + \left(\phi^m\rho_w^m - \phi^m S_w^m\rho_w^m c_w|p_c^m|\right)\frac{\partial S_w^m}{\partial t} - S_w^m\rho_w^m\frac{S}{K}\frac{\partial\sigma_m'}{\partial t}\Big]\widetilde{S_w^m}dV + \sum_{E\in\mathcal{T}}\int_E\lambda_w^m\left(|p_c^m|\nabla S_w^m - \nabla p_{nw}^m\right)\nabla\widetilde{S_w^m}dV - \sum_{e\in\Gamma_m\cup\Gamma_s}\int_e\lambda_w^m\left(|p_c^m|\{\nabla S_w^m\}\right.$$
$$\left. - \langle\nabla p_{nw}^m\rangle\right)[\![\widetilde{S_w^m}]\!]dS + \omega_{ms}\sum_{e\in\Gamma_m\cup\Gamma_s}\int_e\lambda_w^m|p_c^m|\left\{\nabla\widetilde{S_w^m}\right\}[\![S_w^m]\!]dS + \sum_{e\in\Gamma_m\cup\Gamma_s}\int_e\frac{\delta_{ms}}{h}[\![S_w^m]\!]\cdot[\![\widetilde{S_w^m}]\!]dS + \omega_{ms}\sum_{e\in\Gamma_m\cup\Gamma_p}\int_e\lambda_w^m\left\{\nabla\widetilde{S_w^m}\right\}[\![p_{nw}^m]\!]dS$$
$$+ \sum_{e\in\Gamma_m\cup\Gamma_p}\int_e\frac{\delta_{ms}}{h}[\![p_{nw}^m]\!]\cdot[\![\widetilde{S_w^m}]\!]dS + \sum_{e\in\Gamma_f}\int_e\rho_{nw}^{m+}\boldsymbol{v}_{\boldsymbol{w}}^{\boldsymbol{m}+}\bullet\boldsymbol{n}^+\widetilde{S_w^{m+}} + \rho_{nw}^{m-}\boldsymbol{v}_{\boldsymbol{w}}^{\boldsymbol{m}-}\bullet\boldsymbol{n}^-\widetilde{S_w^{m-}}dS = \sum_{e\in\Gamma_q}\int_e\overline{q_w}\widetilde{S_w^m}dS + \omega_{ms}\sum_{e\in\Gamma_s}\int_e\lambda_w^m|p_c^m|\nabla\widetilde{S_w^m}\cdot\boldsymbol{n}\overline{S_w^m}dS$$
$$+ \sum_{e\in\Gamma_s}\int_e\frac{\delta_{ms}}{h}\overline{S_m}\widetilde{S_w^m}dS + \omega_{ms}\sum_{e\in\Gamma_p}\int_e\lambda_w^m\nabla\widetilde{S_w^m}\cdot\boldsymbol{n}\overline{p_{nw}}dS + \sum_{e\in\Gamma_p}\int_e\frac{\delta_{ms}}{h}\overline{p_{nw}}\widetilde{S_w^m}dS \tag{29}$$

and

$$\sum_{E\in\mathcal{T}}\int_E\left(\phi^m S_{nw}^m\rho_{nw}^m c_{nw}\frac{\partial p_{nw}^m}{\partial t} - \phi^m\rho_{nw}^m\frac{\partial S_{nw}^m}{\partial t} - S_{nw}^m\rho_{nw}^m\frac{S}{K}\frac{\partial\sigma_m'}{\partial t}\right)\widetilde{p_{nw}^m}dV + \sum_{E\in\mathcal{T}}\int_E\lambda_{nw}^m\nabla p_{nw}^m\cdot\nabla\widetilde{p_{nw}^m}dV - \sum_{e\in\Gamma_m\cup\Gamma_p}\int_e\lambda_{nw}^m\nabla p_{nw}^m\cdot\nabla\widetilde{p_{nw}^m}dS + \omega_{mp}\sum_{e\in\Gamma_m\cup\Gamma_p}\int_e\lambda_{nw}^m\left\{\nabla\widetilde{p_{nw}^m}\right\}[\![p_{nw}^m]\!]dS$$
$$+ \sum_{e\in\Gamma_m\cup\Gamma_p}\int_e\frac{\delta_{mp}}{h}[\![p_{nw}^m]\!]\cdot[\![\widetilde{p_{nw}^m}]\!]dS + \sum_{e\in\Gamma_f}\int_e\rho_{nw}^{m+}\boldsymbol{v}_{\boldsymbol{nw}}^{+}\bullet\boldsymbol{n}^+\widetilde{p_{nw}^{m+}} + \rho_{nw}^{m-}\boldsymbol{v}_{\boldsymbol{nw}}^{-}\bullet\boldsymbol{n}^-\widetilde{p_{nw}^{m-}}dS = \sum_{e\in\Gamma_q}\int_e\overline{q_{nw}}\widetilde{p_{nw}^m}dS + \omega_{mp}\sum_{e\in\Gamma_s}\int_e\lambda_{nw}^m\nabla\widetilde{p_{nw}^m}\cdot\boldsymbol{n}\overline{p_{nw}}dS$$
$$+ \sum_{e\in\Gamma_s}\int_e\frac{\delta_{mp}}{h}\overline{p_{nw}}\widetilde{p_{nw}^m}dS \tag{30}$$

The mass exchange between the matrix and immersed fracture tip is omitted for the purpose of simplicity since the size of the immersed fracture tip is assumed to be extremely tiny (Kadeethum et al., 2020a). The weak forms with continuous Galerkin approximation for the fluid flow in the deformable fractures are by described by

$$\sum_{e\in\Gamma_f}\int_e\Big[d^f\phi^f S_w^f\rho_w^f c_w\frac{\partial p_{nw}^f}{\partial t} + d^f\left(\phi^f\rho_w^f - \phi^f S_w^f\rho_w^f c_w|p_c^f|\right)\frac{\partial S_w^f}{\partial t} + d^f\alpha\rho_w^f S_w^f\frac{\partial\varepsilon_n}{\partial t}$$
$$- [\![\rho_w^m\boldsymbol{v}_{\boldsymbol{w}}^{\boldsymbol{m}}]\!]\Big]\widetilde{S_w^f}dS + \sum_{e\in\Gamma_f}\int_e d^f\lambda_w^f|p_c^f|\nabla_\tau S_w^f\cdot\nabla_\tau\widetilde{S_w^f}dS$$
$$- \sum_{e\in\Gamma_f}\int_e d^f\lambda_w^f\nabla p_{nw}^f\cdot\nabla_\tau\widetilde{S_w^f}dS = 0 \tag{31}$$

$$\sum_{e\in\Gamma_f}\int_e\Big[d^f\phi^f S_{nw}^f\rho_{nw}^f c_{nw}\frac{\partial p_{nw}^f}{\partial t} - d^f\phi^f\rho_{nw}^f\frac{\partial S_{nw}^f}{\partial t} + d^f\alpha\rho_{nw}^f S_{nw}^f\frac{\partial\varepsilon_n}{\partial t} - [\![\rho_{nw}^m\boldsymbol{v}_{\boldsymbol{nw}}^{\boldsymbol{m}}]\!]\Big]\widetilde{p_{nw}^f}dS$$
$$+ \sum_{e\in\Gamma_f}\int_e d^f\lambda_{nw}^f\nabla_T p_{nw}^f\cdot\nabla_\tau\widetilde{p_{nw}^f}dS = 0 \tag{32}$$

where $\widetilde{\boldsymbol{u}}$, $\widetilde{S_w^\theta}$ and $\widetilde{p_{nw}^\theta}$ are the test functions, h is the mesh size, G is the shear modulus. λ_β^θ is defined as $-\rho_\beta^\theta\frac{\boldsymbol{k}^\theta\boldsymbol{k}_{r\beta}^\theta}{\mu_\beta}$, the parameters $\omega_s = 0$, $\omega_{ms} = 1$, and $\omega_{mp} = 1$ are chosen, resulting in the implementation of the incomplete interior penalty Galerkin (IIPG) method and the nonsymmetric interior penalty Galerkin (NIPG) method are adopted for the fluid and solid equations, respectively (Epshteyn and Rivière, 2007; Liu et al., 2009), the parameters penalty $\delta_s = 10$, $\delta_{ms} = 1$ and $\delta_{mp} = 1$ are provided (Epshteyn and Rivière, 2007; Liu et al., 2009). $[\![\cdot]\!]$ and $\{\cdot\}$ denote the jump and average operators,

$$[\![x]\!] = x^+\boldsymbol{n}^+ + x^-\boldsymbol{n}^-,\ [\![\boldsymbol{x}]\!] = x^+\cdot\boldsymbol{n}^+ + x^-\cdot\boldsymbol{n}^- \tag{33}$$

$$\{x\} = \frac{1}{2}(x^+ + x^-),\ \{\boldsymbol{x}\} = \frac{1}{2}(\boldsymbol{x}^+ + \boldsymbol{x}^-) \tag{34}$$

where x and $\boldsymbol{x}$ denote a scalar and a vector, respectively. For a common boundary shared by two adjacent elements E^+ and E^-, we specify the orientation of the normal unit vector $\boldsymbol{n}$ from E^+ to E^- such that $\boldsymbol{n} = \boldsymbol{n}^+ = -\boldsymbol{n}^-$.

3. Model implementation

In this study, we use COMSOL Multiphysics, a finite element software, to solve the governing equations related to solid deformation and two-phase flow in fractured porous media. Specifically, the weak forms (29)–(30) and (31)–(32) of fluid flow in matrix and fracture are implemented and solved by means of the built-in modulus Weak Form PDE and Weak Form Boundary PDE. Weak Form PDE is used to solve the governing equation of solid deformation. For solving the geomechanical equation and fluid flow in the matrix, the shape function of

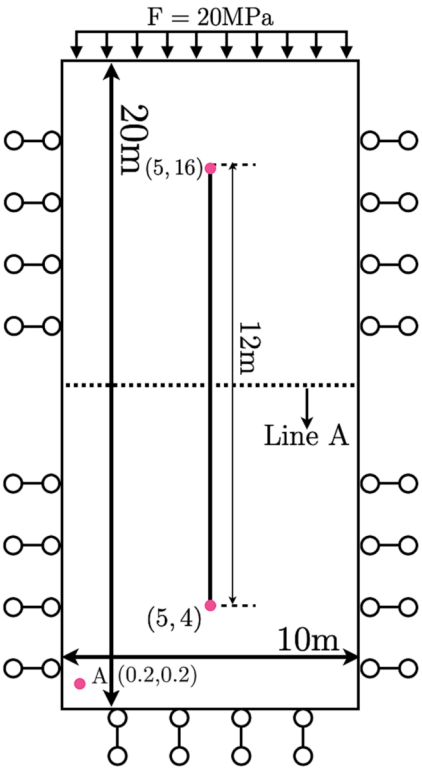

Fig. 4. The geometry and boundary conditions for test case 2. A single vertical fracture is embedded in a rectangle domain. Boundary conditions for solid deformation include loading at the top boundary and fixed displacement in the normal directions at other boundaries. The flow boundaries include zero pressure at the top edges, and no flow conditions at the remaining boundaries.

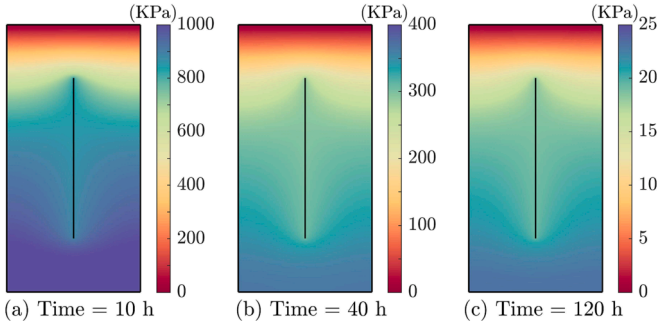

Fig. 5. The pore pressure distribution at three different times t = 10 h, 40 h, and 120 h.

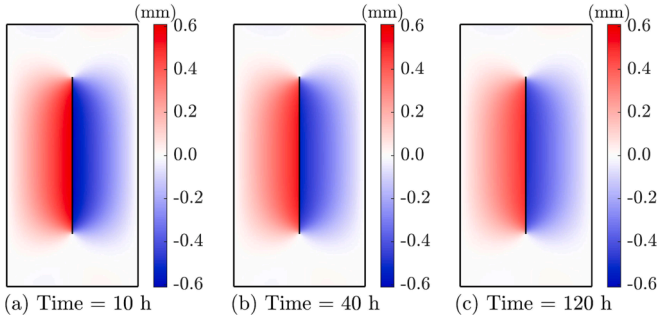

Fig. 6. The horizontal displacement distribution at three different times t = 10 h, 40 h, and 120 h.

discontinuous Lagrange with second-order discretization is chosen. The second-order square quadrilateral Lagrange is utilized for fluid flow equations in fracture. We employ an implicit time-stepping method that utilizes a Backward Differentiation Formula (BDF) along with adaptive time-stepping algorithms for time discretization. Unlike pre-established time-stepping methods, which randomly select time steps, our approach begins with an initial step that is 0.1% of the designated end time. This allows for greater flexibility, as it eliminates the need for redundant time step histories when the end time is modified. It is important to note that altering the time step should not significantly affect the results, provided the tolerance is sufficiently tight to enable automatic time step control. The accuracy of our BDF-based discretization spans a range of one (equivalent to backward Euler) to five. In terms of solving the resulting linear system, we employ the Multifrontal Massively Parallel Sparse (MUMPS) direct solver. Additionally, we opt for a fully coupled solver suitable for nonlinear problems, which is implemented through Newton single-step method. Throughout each Newton iteration, we maintain constant settings and specify a consistent damping factor to ensure stable and accurate solutions.

4. Numerical examples

We present four test cases to assess the performance of the proposed discontinuous and continuous Galerkin method in simulating coupled multiphase flow and geomechanics in fractured porous media. Test case 1 replicates the simulated case from the references (Réthoré et al., 2007; Cusini et al., 2021). In this case, a square domain contains a highly permeable fracture with zero stiffness. (Fig. 2). Test case 2 replicates a simulation case from the references (Yan et al., 2019; Damirchi et al., 2022) with a highly permeable vertical fracture embedded in a rectangular zone exposed to compression and the fracture stiffness is correctly considered (Fig. 4). Test case 3 reproduces a simulated case from Khoei et al. (2016) which considers a coupled two-phase flow and geomechanics problem, with an emphasis on the fracture mechanical characteristics (Fig. 8). Test case 4 models the coupled two-phase flow and geomechanics in a 2D discrete fracture reservoir, incorporating high permeability fractures, low permeability fractures and fracture stiffness (Fig. 11).

4.1. Test case 1: injection in a saturated porous media with an inclined fracture

A saturated reservoir of 10 m by 10 m with a single inclined fracture of 2 m-long located in the middle of the matrix domain is modeled (Fig. 2). The initial reservoir pressure is 0MPa. The fluid is injected from the bottom boundary with a constant rate of 10^{-4}m/s and a constant pressure of 0MPa is supplied to the top surface. Other boundaries are set as no-flow conditions. The top boundary is imposed with free displacement, while the remaining boundaries have zero normal displacements. The overall simulation time is 10 s.

We reproduce the case described in the references (Réthoré et al., 2007; Cusini et al., 2021), which requires mechanical equilibrium and continuous pressure on the fracture surface. We assume that the surfaces of the opening fracture are traction free, meaning that mobilized traction is exclusively associated with the fluid pressure inside the fracture. The coupled single-phase flow and geomechanics modeling are calculated using the DG-CG scheme. Fig. 3 depicts the spatial distribution of vertical displacement for three different scenes at t = 10 s. In the absence of a fracture in porous media, a uniform vertical displacement distribution is obtained. With fluid injection from the bottom boundary, the fluid propagates into the porous matrix and fracture, increasing the pore pressure throughout the porous media and inside the fracture rupture. The increase in fracture pressure enlarges the aperture of fracture and vertical displacement. The reduction in angle θ leads to a significant increase in vertical displacement. This phenomenon can be attributed to

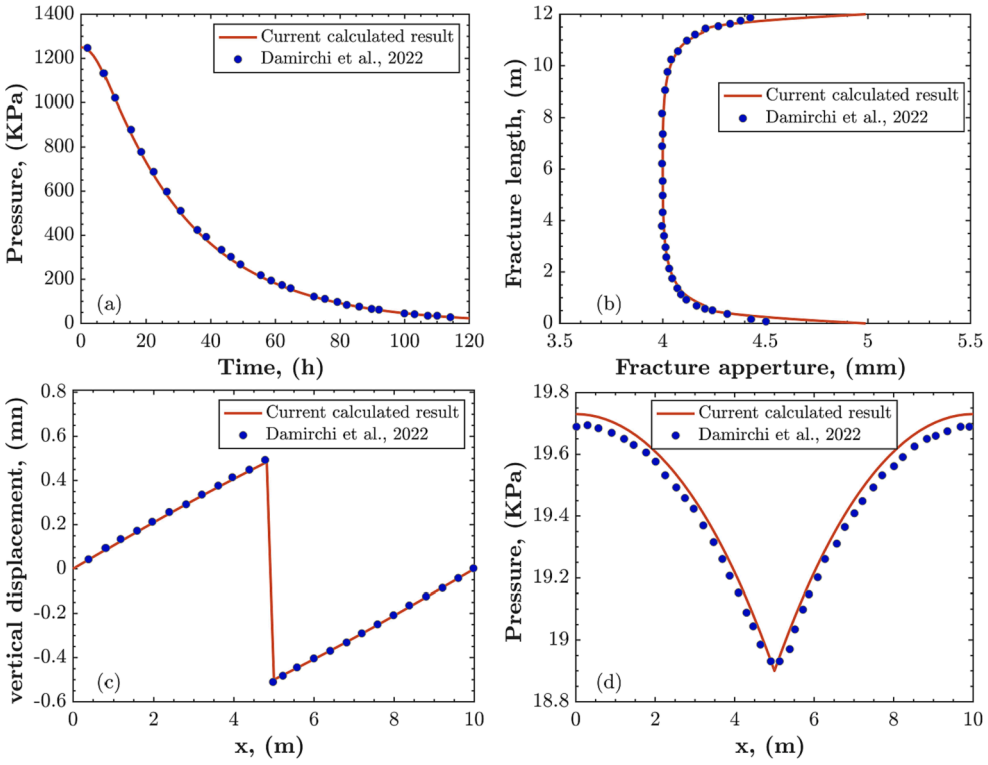

Fig. 7. Comparison of calculated and reference results (Damirchi et al., 2022) (at t = 120 h): (a) evolution of pore pressure at point A, (b) aperture along the fracture, (c) vertical displacement and (d) pore pressure along the line A (shown in Fig. 4) at the end of the simulation. The red line refers to the current calculated results, while the blue dots represent the reference results. (For interpretation of the references to color in this figure legend, the reader is referred to the web version of this article.)

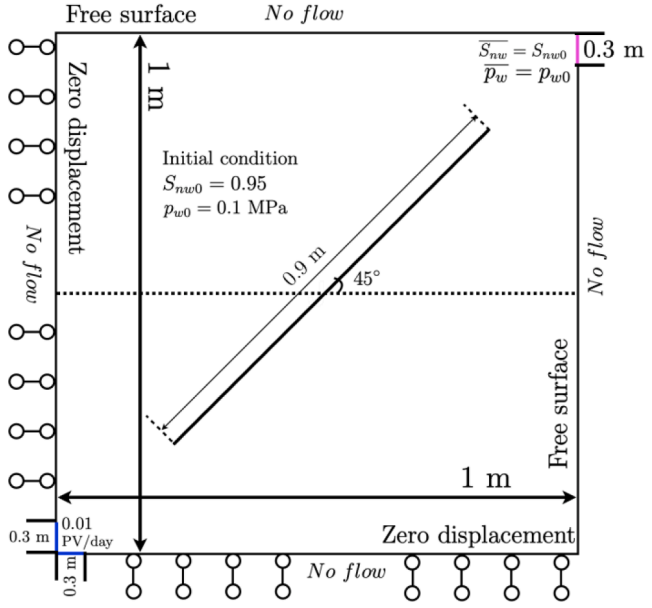

Fig. 8. The geometry and boundary conditions for the test case 3. A 45-degree angle fracture is embedded in a square domain. The left and bottom boundaries are fixed, whereas the right and top boundaries are free surfaces. At the surrounding boundary, no flow boundary condition is applied. The production and injection boundaries are situated in the upper-right and lower-left corners, respectively.

a portion of the fluid accumulating within the fracture, which subsequently leads to a decrease in fluid flow at lower fracture angles. The finding is in accordance with the result from Réthoré et al. (2007) and Cusini et al. (2021) utilizing embedded finite element method (EFEM) and an XFEM-based scheme, respectively.

4.2. Test case 2: coupled hydro-mechanical problem with a single vertical fracture

Fig. 4 depicts a 10 m × 20 m rectangular porous medium with a 12 m long vertical fracture in the center of the domain. The top boundary is subjected to a load of 20 MPa, whereas other boundaries have a fixed displacement in the normal directions. The initial reservoir pressure and fluid pressure at the top boundary are both set to zero. There are no flow conditions applied to the other boundaries.

Following is a summary of the hydro-mechanical properties: Young's modulus and Poisson's ratio of the domain are 10 GPa and 0.2, respectively. The porous media has a porosity of 0.2 and a permeability of 10^{-10} m^2. The initial aperture of fracture is 5 mm that provides an initial fracture-matrix permeability ratio (Matthäi and Nick, 2009) in the order of 10^4. The Biot's coefficient α is 0.75. Consideration is given to the mechanical parameters of the vertical fracture. Stiffness in both normal and shear directions is 4 MPa/mm. The total simulation time is 120 h.

Figs. 5 and 6 depict the spatial distributions of pore pressure and horizontal displacement, respectively. The instantaneous loading on the top boundary causes the water to drain from the domain, reducing the pore pressure. The subsequent reduction in pore pressure cause compaction and corresponding horizontal displacements in the region. Fig. 7 compares the simulated and reference results of the evolution of pore pressure at Point A, as well as the fracture aperture, vertical displacement and pore pressure along the line A (displayed in Fig. 4) at the end of the simulation. A displacement discontinuity is captured between the two sides of the fracture. Throughout the duration of the simulation, the pressure at point A decreases from about 1250 KPa to 23 KPa. The fracture aperture reduces from 5 mm at the fracture tips to

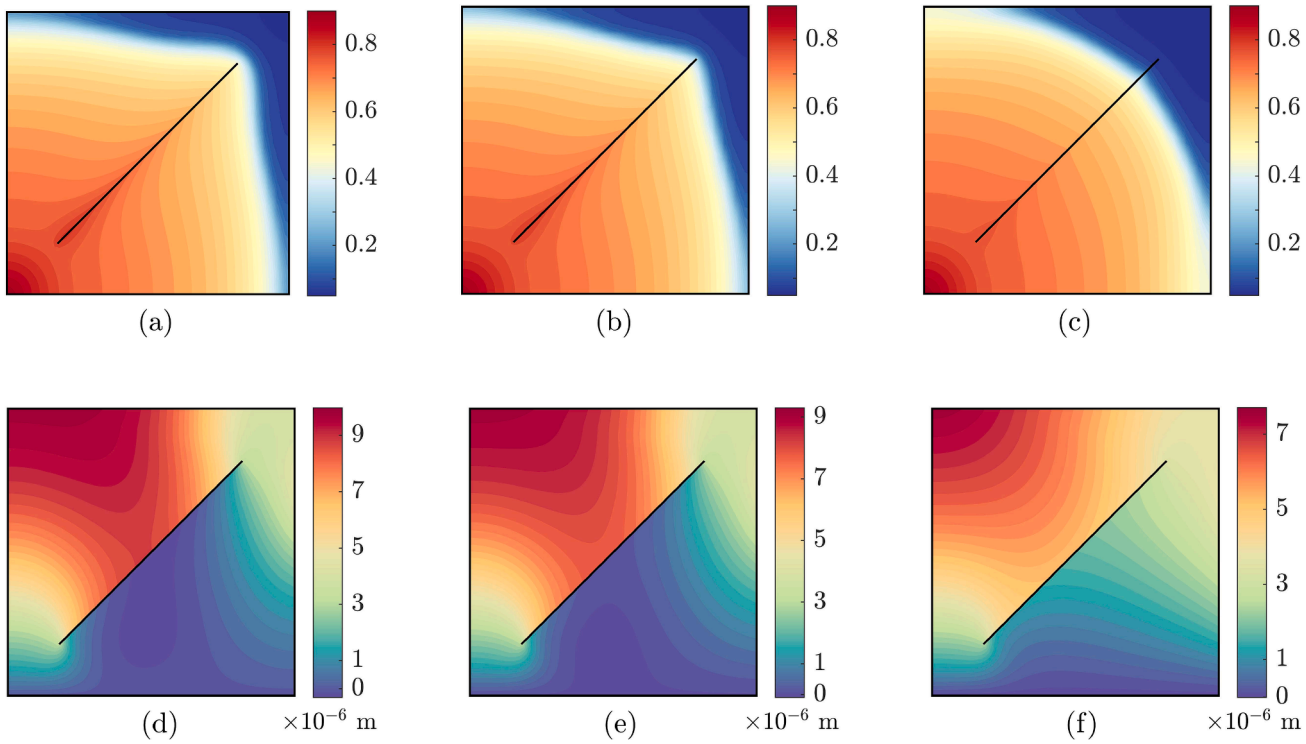

Fig. 9. The spatial distribution of (a)-(c) water saturation and (d)-(f) vertical displacement for three different cases at t = 50 days. The stiffness in the three cases are set to 0, 1, and 10 GPa/m.

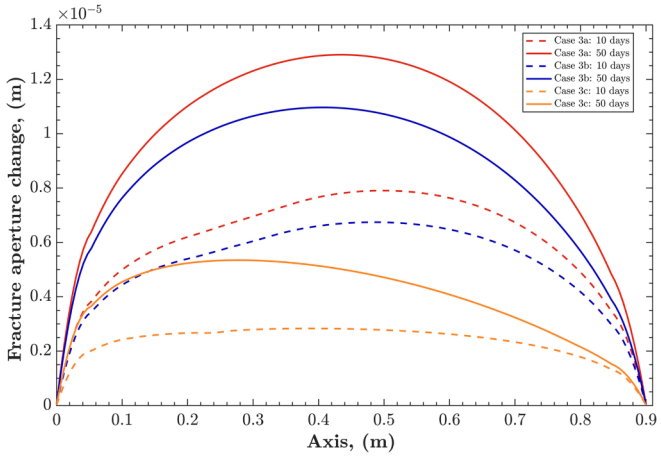

Fig. 10. Profiles of the fracture aperture size along the fracture for three different cases at time = 10 and 50 days. The stiffness in the three cases is set to 0, 1, and 10 GPa/m.

about 4 mm in the central area resulting in almost halving the fracture permeability. This still results in high permeable fracture which cause the pressure decreases gradually from the lateral boundaries to the center of the monitoring line. Obviously, the fracture-matrix permeability contrasts and the distance of the top fracture tip from the open flow boundary control the rate at which the porous media is pressure depleted. While, the existence of a fracture causes a jump in displacement, indicating compression-induced narrowing of the fracture aperture. The comparisons between the results of the reference method (Yan et al., 2019; Damirchi et al., 2022) and the current model are satisfactory.

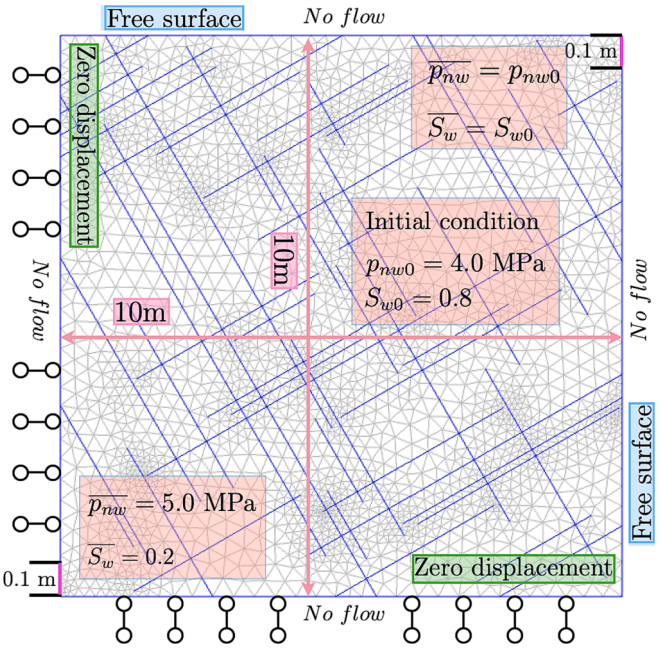

Fig. 11. The geometry, mesh, initial, and boundary conditions for the test case 4. A discrete fracture network is considered inside the reservoir. The left and bottom boundaries are placed with zero displacements, while the right and top boundaries are free surfaces. No flow boundary condition is applied at the surrounding boundary. The injection and production wells positioned in the bottom-left and top-right and corners, respectively, are subjected to constant pressure and saturation. The domain is initially saturated with water ($S_w = 0.8$) and CO_2 ($S_{nw} = 0.2$).

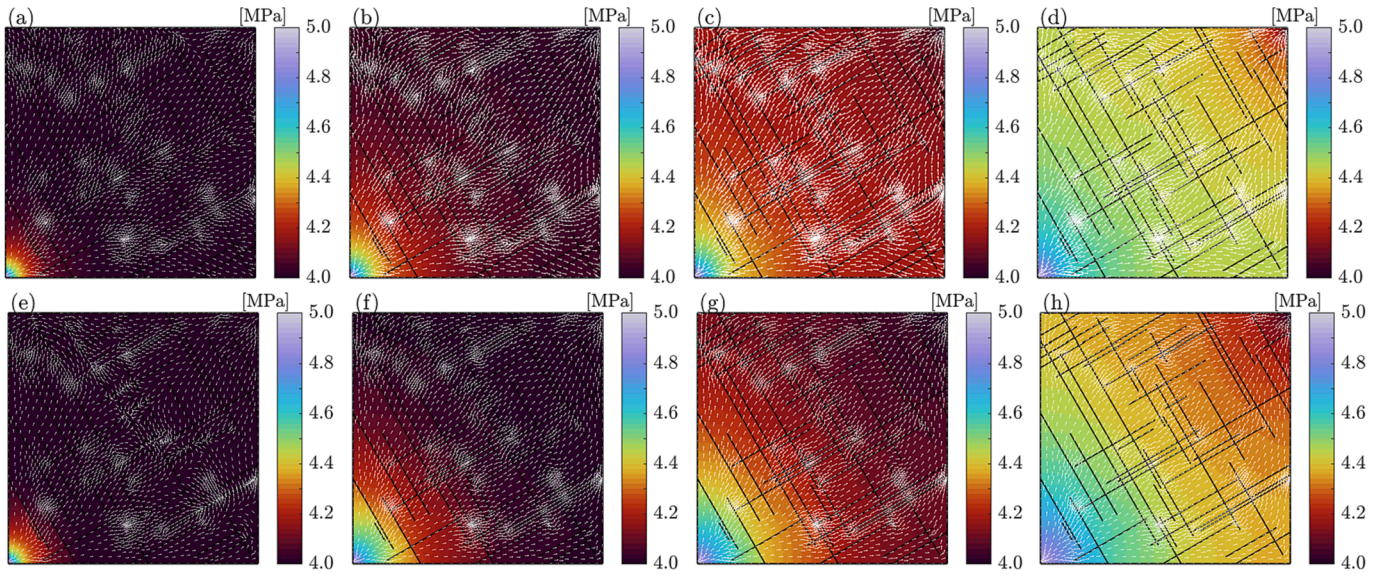

Fig. 12. The spatial distribution of non-wetting phase pressure at four-time steps t = 0.01, 0.10, 0.30, and 1.00 h for two cases. (a)-(d) depict the results of case 4a, and (e)-(h) depict the results of case 4b. All figures are rendered with the same color scale.

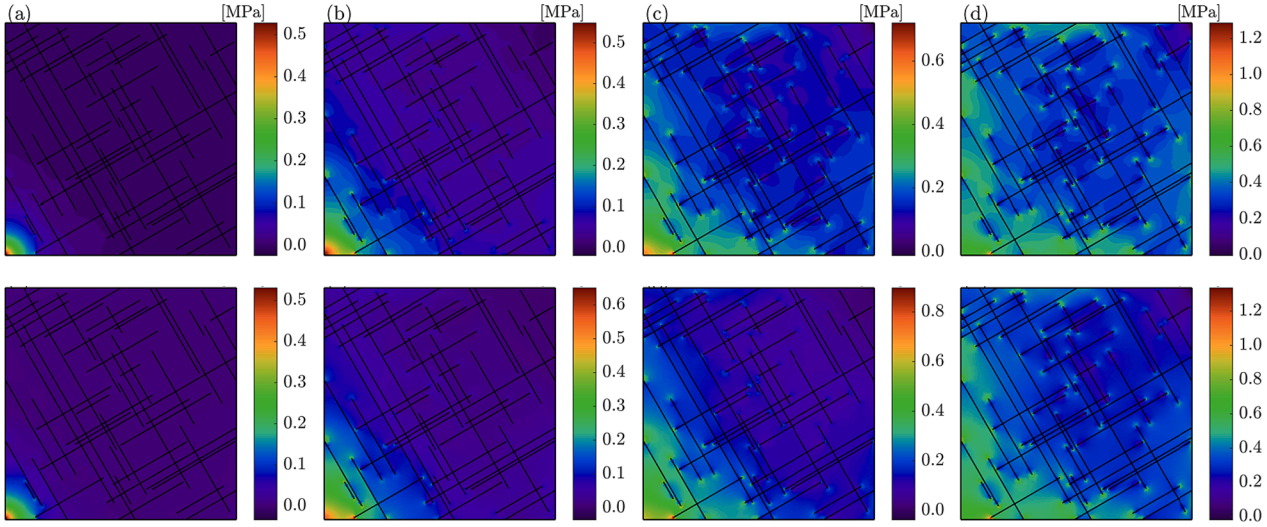

Fig. 13. The spatial distribution of the mean effective stress changes at four-time steps t = 0.01, 0.10, 0.30 and 1.00 h for two cases. (a)-(d) are the results of case 4a, and (e)-(h) are the results of case 4b. Each figure is assigned a specific color scale.

4.3. Test case 3: water injection into a fractured porous medium

As seen in Fig. 8, a 0.9 m long fracture is inserted in a square porous medium of $1m \times 1m$ initially fully saturated with oil. The fracture is oriented at 45-dgree angle. The mechanical boundaries consist of free surface on the top and right and zero-displacement on the bottom and left. All the boundaries are configured as no-flow boundaries. The water pressure of initial reservoir and production boundary is 0.1 MPa, while the oil saturation of initial reservoir and production boundary is 0.95. The water is injected from the inlet boundaries at a rate of 0.01 PV/day for 50 days.

The hydromechanical characteristics are listed below: the density and viscosity of water are 1000 kg/m^3 and 1×10^{-3}Pa • S, the density and viscosity of oil are 600 kg/m^3 and 0.45×10^{-3}Pa • S. For the matrix, the porosity and permeability are 0.2 and $9.87 \times 10^{-16}m^2$(1 mD), and the Young's modulus and Poisson's ratio are 10 GPa and 0.2. Assuming the fracture has a porosity of 1, the initial aperture of 1.00×10^{-6}m corresponds to an initial fracture permeability of $8.33 \times 10^{-14}m^2$. The initial fracture-matrix permeability ratio is equal to 84.4 which is lower than that of the previous case. Other parameters are sourced from the reference (Khoei et al., 2016). As highlighted in the previous publications, the sharp contrast between the fracture and matrix flow properties demands special care for the fracture and matrix interfaces (Nick and Matthäi, 2011).

To examine the influence of fracture stiffness on flow behavior and solid deformation, three cases, referred to as cases 3a, 3b, and 3c, are performed. In each case, the normal and shear stiffness have the same value. For cases 3a, 3b and 3c, the stiffnesses are set to 0, 1, and 10 GPa/m, respectively. Fig. 9 illustrates the distribution of saturation and vertical displacement at the end of water injection for the three cases. Fig. 10 shows the aperture along the fracture for three different cases at time = 10 and 50 days. In all three cases, discontinuous displacement is captured between two sides of the fracture. When the stiffness reduces, the fracture opening widens, which causes an augmentation of the corresponding permeability of fracture and hence accelerates the fluid migration through the fracture. As predicted, case 3a exhibits the largest

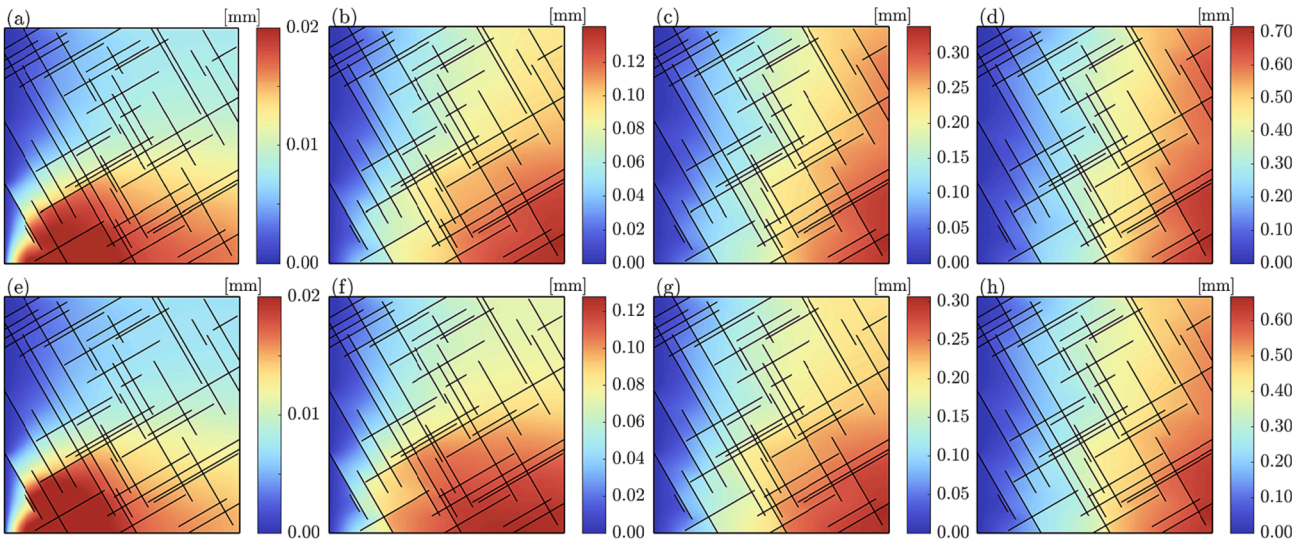

Fig. 14. The spatial distribution of the horizontal displacement changes at four-time steps t = 0.01, 0.10, 0.30, and 1.00 h for two case2. (a)-(d) are the results of case 4a, and (e)-(h) are the results of case 4b. Each figure is assigned a specific color scale.

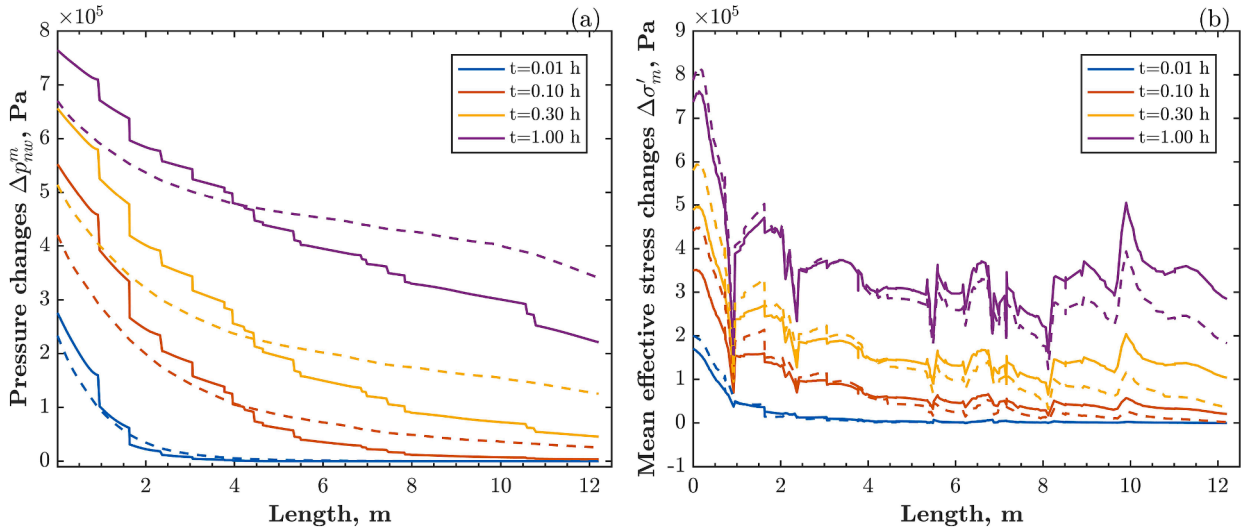

Fig. 15. The changes of non-wetting phase pressure and mean effective stress along the monitoring line at t = 0.01, 0.10, 0.30, and 1.00 h. The simulation results for conducting fracture and blocking barrier are plotted with dash and solid lines.

fracture aperture when fracture stiffness is ignored. After 50 days of injection, the maximum fracture aperture in cases 3a and 3c increase to approximately 14 times and 6.35 times the initial fracture aperture of 1×10^{-6}m, repectively. Overall, the simulation demonstrates conclusively the significance of geomechanical impact on the two-phase flow.

4.4. Test case 4: CO_2 injection into a reservoir with a complex fracture network

A complex configuration with a discrete fracture network is considered for the last case. Two situations with distinct fracture types are considered, namely conducting fractures, and blocking fractures (barriers). In case 4a, the conducting fracture has a greater permeability than the surrounding porous medium while in case 4b, the fractures have a lower permeability.

Fig. 11 illustrates the geometry, mesh, initial conditions, and boundary conditions for case 4. The discrete fracture network is generated by ADFNE software (Fadakar Alghalandis, 2017). The fracture information is imported into the COMSOL Multiphase though a live connection with MATLAB. Initial nonwetting pressure p_{nw0} is 4.0 MPa, and wetting saturation is 0.8. Dirichlet conditions are applied to the injection and production wells. The injection pressure and saturation are 5.0 MPa and 0.2, and the production well maintains the same pressure and saturation as the initial conditions.

The hydromechanical characteristics are summarized as follows: the density and viscosity of water are 1000 kg/m^3 and 1×10^{-3}Pa • S, the density and viscosity of CO_2 are 3.18 kg/m^3 and 9.02×10^{-6}Pa • S. The compressibility of water and CO_2 are 3.84×10^{-10}1/Pa and 7.71×10^{-6}1/Pa. For the matrix, the porosity and permeability are 0.10 and 1.00 $\times 10^{-14}$m^2, and Young's modulus and Poisson's ratio are 10.00 GPa and 0.25. As described before, the fracture has a porosity of 1, an initial aperture of 1.00×10^{-3}m. Initial permeability for conducting and blocking fractures are 1.00×10^{-11}m^2 and 1.00×10^{-17}m^2, resulting in initial fracture-matrix permeability ratios of 10^3 and 10^{-3}. Normal and shear fracture stiffness is equal to 10.00 GPa/m for both cases.

Figs. 12-14 depict the spatial distribution of the variations in non-wetting phase pressure, mean effective stress and the horizontal displacement at t = 0.01, 0.10, 0.30, and 1.00 h for highly permeable

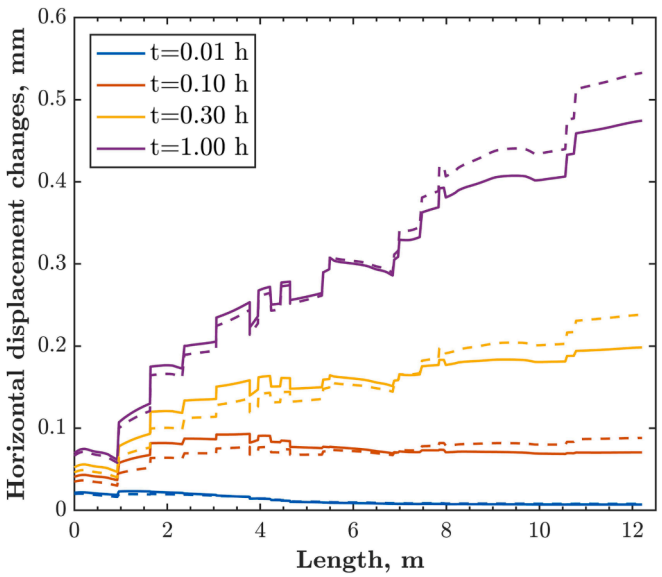

Fig. 16. Horizontal displacement changes along the monitoring line at t = 0.01, 0.10, 0.30, and 1.00 h. The simulation results for conducting fracture and blocking barrier are plotted with dash and solid lines.

fractures and less permeable barriers. As illustrated in Figs. 15 and 16, we assess the variations in pressure, effective stress, and horizontal displacement along the monitoring line. The tip coordinates of the monitoring line segment are (1,0) and (8,10). The simulation result indicates that the internal pressure of reservoir rises when CO_2 is continuously injected. As a result of the varying fracture permeabilities, the prorogation velocity of CO_2 differs between the two cases. The fluid spreads more rapidly in case 4a into the reservoir in cases with higher permeability, leading to a larger pressure gradient. Since a constant injection pressure is supplied to the bottom-left corner, the pressure is reduced at the same position with high-permeability fractures within the zone extending from the injection well to the fracture. This fluid movement is hindered upon encountering a barrier, resulting in diminished pressure behind the barrier. Poroelastic effect is responsible for the change in displacement ahead of the pressure (Lei et al., 2021). The displacement inside the reservoir is caused by the fluctuation in pore pressure created by the simultaneous injection and production process. In Fig. 15(b) and 16, the changes in mean effective stress and horizontal displacement correspond to the evolution of the overpressure. The increase in pressure corresponds to a decrease in effective stress and, consequently, leads to an enhancement in changes of deformation. As a consequence of highly permeable fractures favoring the fluid flow through the fracture, the pressure in case 4a drops smoothly from the injection area to a distant location. In contrast, the fluid is impeded by the low permeability barrier, which results in discontinuous pressure on each side of the barriers. The presence of discrete fractures results in substantial variation in the domains of stress and displacement. With the continued injection, the displacement jumps and stress change around fracture are caused by the dissimilar mechanical characteristics of the facture and matrix.

Fig. 17 shows that spatial distribution of fracture aperture for the two cases and the aperture difference between the two cases at t = 0.01, 0.10, 0.30, and 1.00 h. In the early stage, the fractures oriented at 30° near the injection well undergo substantial opening under the growing pore pressure, which further promotes the aperture widening and the associated permeability enhancement. This is in accordance with the findings of Kadeethum et al (Kadeethum et al., 2019; Kadeethum et al., 2020b). When the pressure spreads inside the reservoir, both the 30° and 120° fractures undergo experience significant opening. More fluid

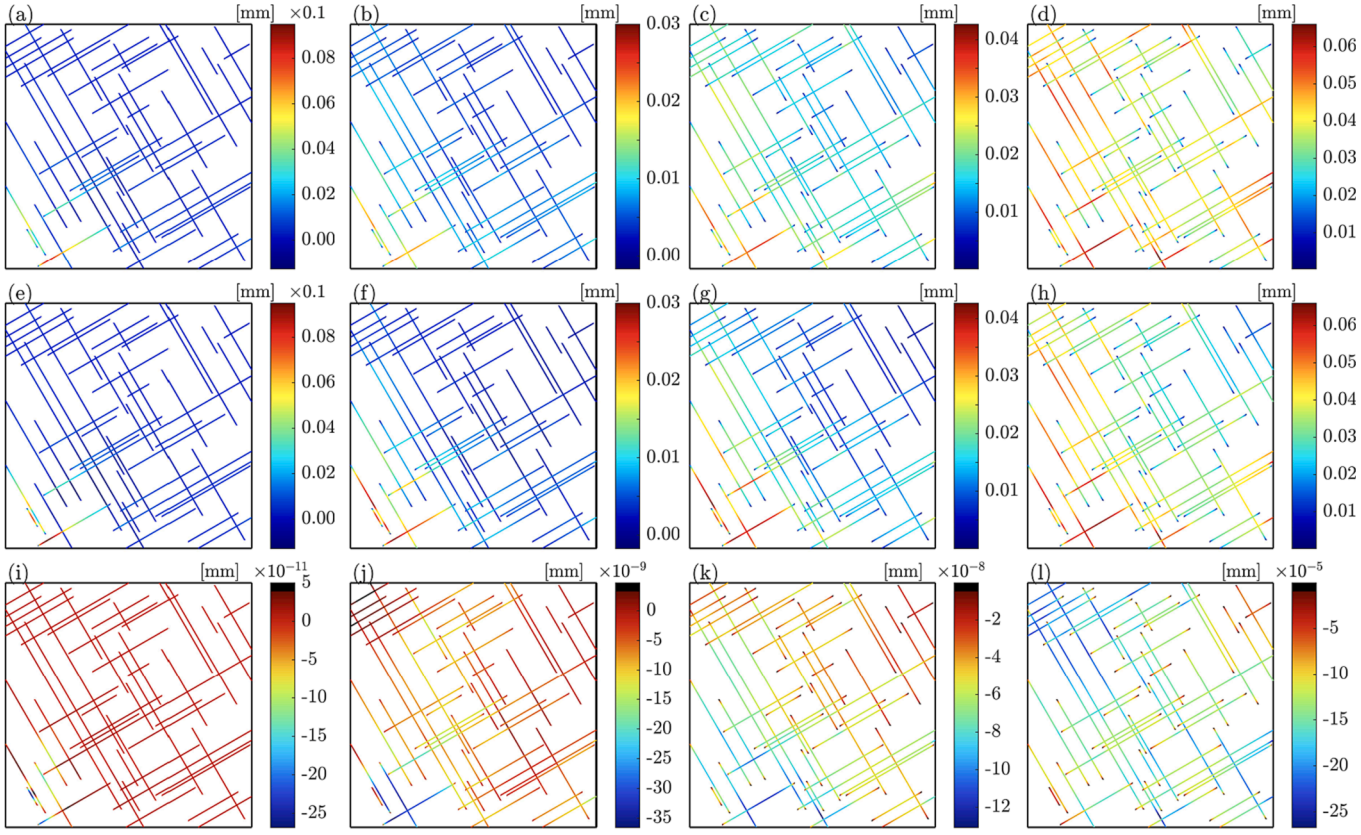

Fig. 17. The spatial distribution of fracture aperture at four selected time steps t = 0.01, 0.10, 0.30, and 1.00 h for two cases. (a)-(d) show the results of case 4a, and (e)-(h) show the results of case 4b, and (i)-(l) show the aperture difference between the two cases. Different color scales are set for all the figures.

migrates into the domain due to the increase in fracture permeability and the connectivity of the fracture network. Throughout the entire simulation, the procedure will recur. Meanwhile, as the pressure difference inside the fractures between case 4a and 4b increases, so does the aperture difference between two of them.

5. Conclusion and summary

In this work, a fully coupled two-phase flow and poromechanics modeling of fractured porous media is presented. Mixed discontinuous Galerkin (DG) and continuous Galerkin (CG) finite element method is utilized to discretize the fluid and solid equations with fractures discretized with lower dimensional entity embedded in the matrix domain. The hydro-mechanical contributions of fractures are captured by employing the discrete fracture models. Multiple benchmark tests are performed to evaluate the accuracy of the proposed numerical approach. The simulated results correspond well with the reference results, demonstrating the accuracy of the proposed method. The governing equations of the proposed coupled model and the associated DG-CG finite element method enable simulations of the coupled problem with and without the mechanical characteristic, as well as conduit and sealed (baffle) fractures. In the case of conducting fractures and blocking barriers, the modeling results indicate a discontinuous and continuous pressure distribution, respectively. Due to the difference in mechanical characteristics between the fracture and the surrounding matrix, displacement jumps are captured between the two sides of fractures. The increase in fracture stiffness enlarges the deformation of the fracture.

Ongoing research focuses on the discontinuous capillary pressure between the matrix and fracture, fracture slip, fault reactivation, and seismicity induced by gas injection or production, with a particular emphasis on the faults constitutive models of slip-weakening friction, rate-and-state friction, and the adoption or development of novel solver strategies.

CRediT authorship contribution statement

Tianran Ma: Conceptualization, Funding acquisition, Methodology, Writing – original draft, Visualization. **Lintong Jiang:** Writing – original draft, Visualization. **Weijun Shen:** Funding acquisition, Writing – review & editing. **WenZhuo Cao:** Formal analysis, Investigation, Writing – review & editing. **Chaobin Guo:** Formal analysis, Funding acquisition, Methodology, Writing – review & editing. **Hamidreza M. Nick:** Methodology.

Declaration of Competing Interest

The authors declare that they have no known competing financial interests or personal relationships that could have appeared to influence the work reported in this paper.

Data availability

Data will be made available on request.

Acknowledgments

We would like to thank Lei Jin from ExxonMobil and Guotong Ren from Chevron for their helpful discussions on the simulation. This study was supported by the National Natural Science Foundation of China (No. 12202483, 12172362, 42002255 and 42372286), PetroChina Innovation Foundation (No. 2021DQ02-0204), and China Postdoctoral Science Foundation (2022M713374), the Chinese Academy of Geological Sciences through Chinese Geological Survey Projects (DD20221819) and the Fund from SinoProbe Laboratory (SinoProbe Lab 202210). This research was partially funded by the Danish Energy Technology Development and Demonstration Program (EUDP), through the Bifrost project (64021-9007).

References

Aghili, J., Brenner, K., Hennicker, J., Masson, R., Trenty, L., 2019. Two-phase Discrete Fracture Matrix models with linear and nonlinear transmission conditions. GEM – Int. J. Geomathem. 10 (1), 1.
Cerfontaine, B., Dieudonné, A.-C., Radu, J.-P., Collin, F., Charlier, R., 2015. 3D zero-thickness coupled interface finite element: Formulation and application. Comput. Geotech. 69, 124–140.
Cusini, M., White, J.A., Castelletto, N., Settgast, R.R., 2021. Simulation of coupled multiphase flow and geomechanics in porous media with embedded discrete fractures. Int. J. Numer. Anal. Meth. Geomech. 45 (5), 563–584.
Damirchi, B.V., Bitencourt, L.A.G., Manzoli, O.L., Dias-da-Costa, D., 2022. Coupled hydro-mechanical modelling of saturated fractured porous media with unified embedded finite element discretisations. Comput. Methods Appl. Mech. Eng. 393, 114804.
Deb, R., Jenny, P., 2017. Modeling of shear failure in fractured reservoirs with a porous matrix. Comput. Geosci. 21 (5), 1119–1134.
Epshteyn, Y., Rivière, B., 2007. Fully implicit discontinuous finite element methods for two-phase flow. Appl. Numer. Math. 57 (4), 383–401.
Fadakar Alghalandis, Y., 2017. ADFNE: Open source software for discrete fracture network engineering, two and three dimensional applications. Comput. Geosci. 102, 1–11.
Fumagalli, A., Scotti, A., 2013. A numerical method for two-phase flow in fractured porous media with non-matching grids. Adv. Water Resour. 62, 454–464.
Gläser, D., Helmig, R., Flemisch, B., Class, H., 2017. A discrete fracture model for two-phase flow in fractured porous media. Adv. Water Resour. 110, 335–348.
Gläser, D., Flemisch, B., Helmig, R., Class, H., 2019. A hybrid-dimensional discrete fracture model for non-isothermal two-phase flow in fractured porous media. GEM – Int. J. Geomathem. 10 (1), 5.
Gläser, D., Schneider, M., Flemisch, B., Helmig, R., 2022. Comparison of cell- and vertex-centered finite-volume schemes for flow in fractured porous media. J. Comput. Phys. 448, 110715.
Goodman, R.E., Taylor, R.L., Brekke, T.L., 1968. A model for the mechanics of jointed rock. J. Soil Mech. Found. Divis. 94 (3), 637–659.
HosseiniMehr, M., Tomala, J.P., Vuik, C., Kobaisi, M.A., Hajibeygi, H., 2022. Projection-based embedded discrete fracture model (pEDFM) for flow and heat transfer in real-field geological formations with hexahedral corner-point grids. Adv. Water Resour. 159, 104091.
Jafari, A., Broumand, P., Vahab, M., Khalili, N., 2022. An eXtended Finite Element Method implementation in COMSOL Multiphysics: Solid Mechanics. Finite Elem. Anal. Des. 202, 103707.
Jiang, J., Yang, J., 2018. Coupled fluid flow and geomechanics modeling of stress-sensitive production behavior in fractured shale gas reservoirs. Int. J. Rock Mech. Min. Sci. 101, 1–12.
Jiang, J., Younis, R.M., 2017. An improved projection-based embedded discrete fracture model (pEDFM) for multiphase flow in fractured reservoirs. Adv. Water Resour. 109, 267–289.
Jin, L., Zoback, M.D., 2017. Fully Coupled Nonlinear Fluid Flow and Poroelasticity in Arbitrarily Fractured Porous Media: A Hybrid-Dimensional Computational Model. J. Geophys. Res. Solid Earth 122 (10), 7626–7658.
Kadeethum, T., Salimzadeh, S., Nick, H.M., 2019. An investigation of hydromechanical effect on well productivity in fractured porous media using full factorial experimental design. J. Pet. Sci. Eng. 181, 106233.
Kadeethum, T., Nick, H.M., Lee, S., Ballarin, F., 2020a. Flow in porous media with low dimensional fractures by employing enriched Galerkin method. Adv. Water Resour. 142, 103620.
Kadeethum, T., Salimzadeh, S., Nick, H.M., 2020b. Well productivity evaluation in deformable single-fracture media. Geothermics 87, 101839.
Khoei, A.R., Hosseini, N., Mohammadnejad, T., 2016. Numerical modeling of two-phase fluid flow in deformable fractured porous media using the extended finite element method and an equivalent continuum model. Adv. Water Resour. 94, 510–528.
Khoei, A.R., Saeedmonir, S., 2021. Computational homogenization of fully coupled multiphase flow in deformable porous media. Comput. Methods Appl. Mech. Eng. 376, 113660.
Latham, J.-P., et al., 2013. Modelling stress-dependent permeability in fractured rock including effects of propagating and bending fractures. Int. J. Rock Mech. Min. Sci. 57, 100–112.
Lei, Q., Gholizadeh Doonechaly, N., Tsang, C.-F., 2021. Modelling fluid injection-induced fracture activation, damage growth, seismicity occurrence and connectivity change in naturally fractured rocks. Int. J. Rock Mech. Min. Sci. 138, 104598.
Liu, L., et al., 2021. Simulating two-phase flow and geomechanical deformation in fractured karst reservoirs based on a coupled hydro-mechanical model. Int. J. Rock Mech. Min. Sci. 137, 104543.
Liu, F., 2022. Modeling fracture propagation in a rock-water-air system with the assumed enhanced strain method. Int. J. Numer. Meth. Eng. 123 (11), 2429–2466.
Liu, R., Wheeler, M.F., Dawson, C.N., Dean, R.H., 2009. On a coupled discontinuous/continuous Galerkin framework and an adaptive penalty scheme for poroelasticity problems. Comput. Methods Appl. Mech. Eng. 198 (41), 3499–3510.
Ma, T., Rutqvist, J., Oldenburg, C.M., Liu, W., Chen, J., 2017. Fully coupled two-phase flow and poromechanics modeling of coalbed methane recovery: Impact of geomechanics on production rate. J. Nat. Gas Sci. Eng. 45, 474–486.

Ma, T., Shen, W., Liu, W., Xu, H., 2021a. Discontinuous Galerkin FEM method for the coupling of compressible two-phase flow and poromechanics. Chin. J. Theor. Appl. Mech. 53 (8), 2235–2245.
Ma, T., Zhang, K., Shen, W., Guo, C., Xu, H., 2021b. Discontinuous and continuous Galerkin methods for compressible single-phase and two-phase flow in fractured porous media. Adv. Water Resour. 156, 104039.
Ma, T., et al., 2020. A discrete fracture modeling approach for analysis of coalbed methane and water flow in a fractured coal reservoir. Geofluids 2020.
Matthäi, S.K., Nick, H.M., 2009. Upscaling two-phase flow in naturally fractured reservoirs. AAPG Bull. 93 (11), 1621–1632.
Matthäi, S.K., Nick, H.M., Pain, C., Neuweiler, I., 2010. Simulation of Solute Transport Through Fractured Rock: A Higher-Order Accurate Finite-Element Finite-Volume Method Permitting Large Time Steps. Transp. Porous Media 83 (2), 289–318.
Monteagudo, J., Firoozabadi, A., 2004. Control-volume method for numerical simulation of two-phase immiscible flow in two-and three-dimensional discrete-fractured media. Water Resour. Res. 40 (7).
Nguyen, V.P., 2014a. Discontinuous Galerkin/extrinsic cohesive zone modeling: Implementation caveats and applications in computational fracture mechanics. Eng. Fract. Mech. 128, 37–68.
Nguyen, V.P., 2014b. An open source program to generate zero-thickness cohesive interface elements. Adv. Eng. Softw. 74, 27–39.
Nick, H.M., Matthäi, S.K., 2011. Comparison of Three FE-FV Numerical Schemes for Single- and Two-Phase Flow Simulation of Fractured Porous Media. Transp. Porous Media 90 (2), 421–444.
Obeysekara, A., et al., 2018. Modelling stress-dependent single and multi-phase flows in fractured porous media based on an immersed-body method with mesh adaptivity. Comput. Geotech. 103, 229–241.
Pruess, K., Oldenburg, C.M. and Moridis, G., 1999. TOUGH2 user's guide version 2, Lawrence Berkeley National Lab.(LBNL), Berkeley, CA (United States).
Reichenberger, V., Jakobs, H., Bastian, P., Helmig, R., 2006. A mixed-dimensional finite volume method for two-phase flow in fractured porous media. Adv. Water Resour. 29 (7), 1020–1036.
Ren, G., Jiang, J., Younis, R.M., 2018. A Model for coupled geomechanics and multiphase flow in fractured porous media using embedded meshes. Adv. Water Resour. 122, 113–130.
Ren, G., Younis, R.M., 2021. An integrated numerical model for coupled poro-hydro-mechanics and fracture propagation using embedded meshes. Comput. Methods Appl. Mech. Eng. 376, 113606.
Réthoré, J., Borst, R.D., Abellan, M.-A., 2007. A two-scale approach for fluid flow in fractured porous media. Int. J. Numer. Methods Eng. 71 (7), 780–800.
Salimzadeh, S., Paluszny, A., Nick, H.M., Zimmerman, R.W., 2018. A three-dimensional coupled thermo-hydro-mechanical model for deformable fractured geothermal systems. Geothermics 71, 212–224.
Salimzadeh, S., Grandahl, M., Medetbekova, M., Nick, H.M., 2019a. A novel radial jet drilling stimulation technique for enhancing heat recovery from fractured geothermal reservoirs. Renew. Energy 139, 395–409.
Salimzadeh, S., Hagerup, E.D., Kadeethum, T., Nick, H.M., 2019b. The effect of stress distribution on the shape and direction of hydraulic fractures in layered media. Eng. Fract. Mech. 215, 151–163.
Segura, J.M., Carol, I., 2008. Coupled HM analysis using zero-thickness interface elements with double nodes. Part I: Theoretical model. Int. J. Numer. Anal. Meth. Geomech. 32 (18), 2083–2101.
Shen, B., Riviere, B., 2022. A sequential discontinuous Galerkin method for two-phase flow in deformable porous media. Comput. Methods Appl. Mech. Eng. 399, 115266.
Tian, J., Liu, J., Elsworth, D., Leong, Y.-K., 2023. A 3D hybrid DFPM-DFM Model for gas production from fractured shale reservoirs. Comput. Geotech. 159, 105450.
Wang, Y., Vuik, C., Hajibeygi, H., 2022. CO_2 Storage in deep saline aquifers: impacts of fractures on hydrodynamic trapping. Int. J. Greenhouse Gas Control 113, 103552.
Wu, W., Yang, Y., Zheng, H., 2020. Hydro-mechanical simulation of the saturated and semi-saturated porous soil–rock mixtures using the numerical manifold method. Comput. Methods Appl. Mech. Eng. 370, 113238.
Yan, X., et al., 2019. Numerical simulation of hydro-mechanical coupling in fractured vuggy porous media using the equivalent continuum model and embedded discrete fracture model. Adv. Water Resour. 126, 137–154.
Zheng, S., Li, S., Zhang, D., 2021. Fluid and heat flow in enhanced geothermal systems considering fracture geometrical and topological complexities: An extended embedded discrete fracture model. Renew. Energy 179, 163–178.